Electronic Supplementary Material (ESI) for Journal of Materials Chemistry A.
This journal is © The Royal Society of Chemistry 2018

Supporting Information

Hierarchical 3D Zn-Ni-P nanosheet arrays as an advanced electrode for high-performance all-solid-state asymmetric supercapacitors

Thanh Tuan Nguyen,[a] Jayaraman Balamurugan,[a] Nam Hoon Kim,[a] and Joong Hee Lee[a,b*]

[a]Advanced Materials Institute of BIN Convergence Technology (BK21 Plus Global) & Dept. of BIN Convergence Technology, Chonbuk National University, Jeonju, Jeonbuk 54896, Republic of Korea.

[b]Carbon Composite Research Centre, Department of Polymer –Nano Science and Technology, Chonbuk National University, Jeonju, Jeonbuk 54896, Republic of Korea

---

**Corresponding author:* Tel: +82-63-270-2342

Email address: jhl@jbnu.ac.kr (Joong Hee Lee)

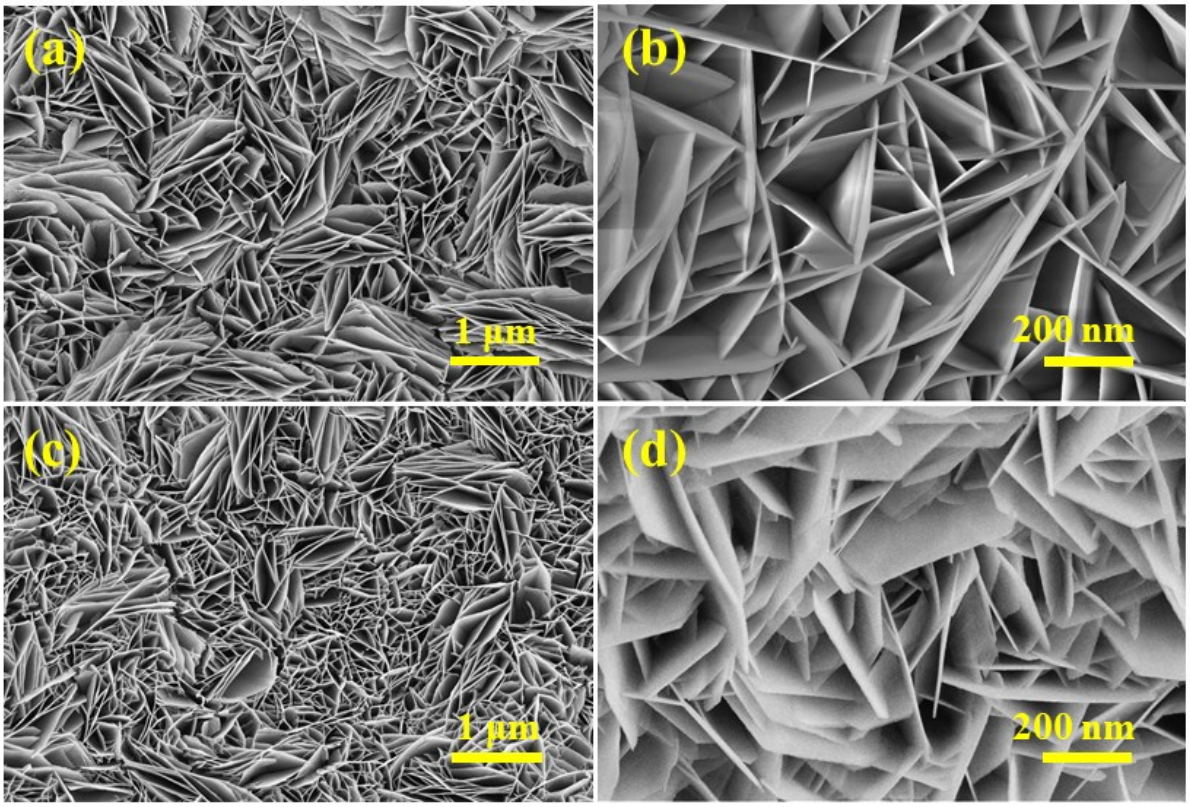

Fig. S1 (a, b) SEM images with different magnification of Zn-Ni LDH precursors, and (c, d) SEM images with different magnification of Zn-Ni-O NS arrays.

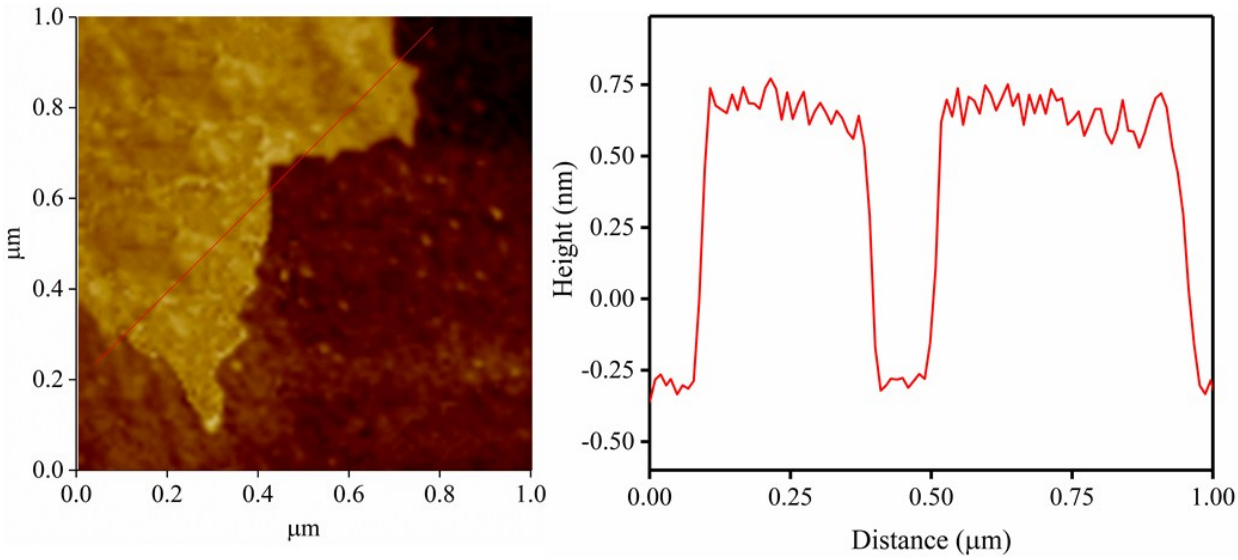

Fig. S2 AFM image and its height profile of Zn-Ni-P NS arrays.

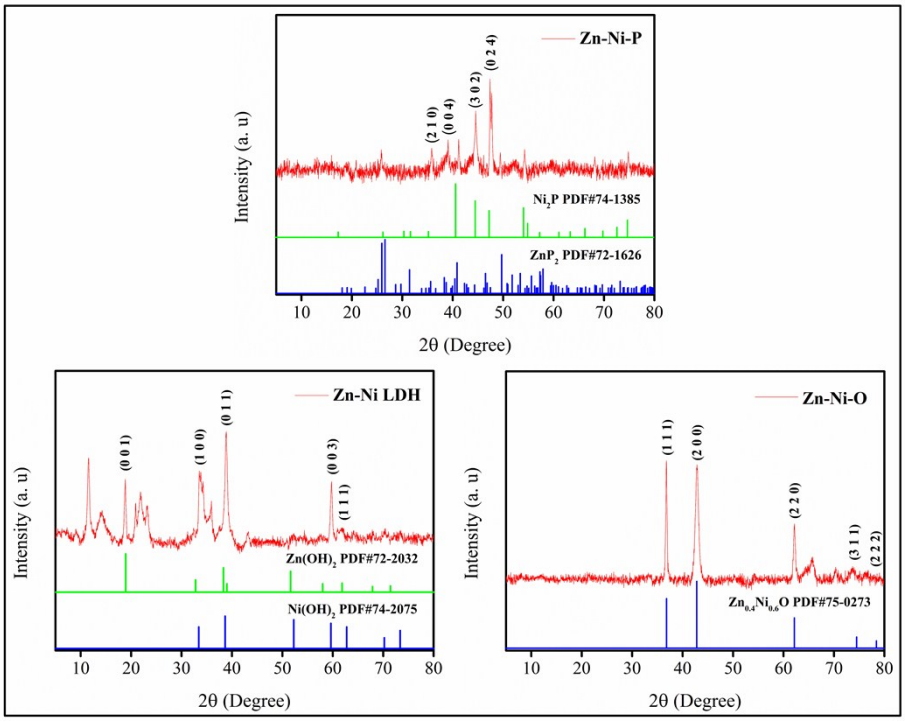

Fig. S3 X-ray diffraction pattern of Zn-Ni-P, Zn-Ni LDH, and Zn-Ni-O NS arrays.

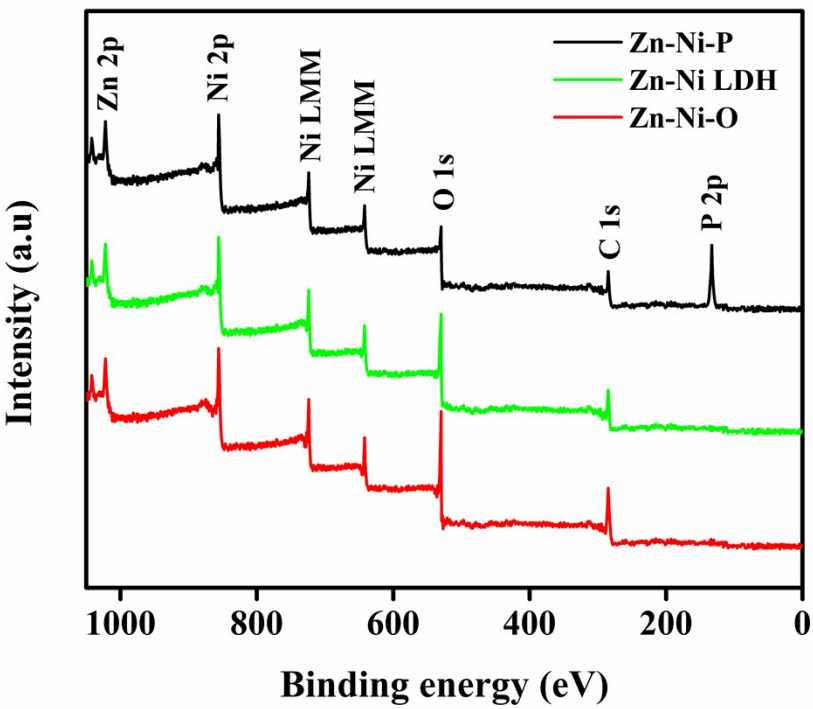

Fig. S4 XPS survey spectra of Zn-Ni-P, Zn-Ni LDH, and Zn-Ni-O NS arrays.

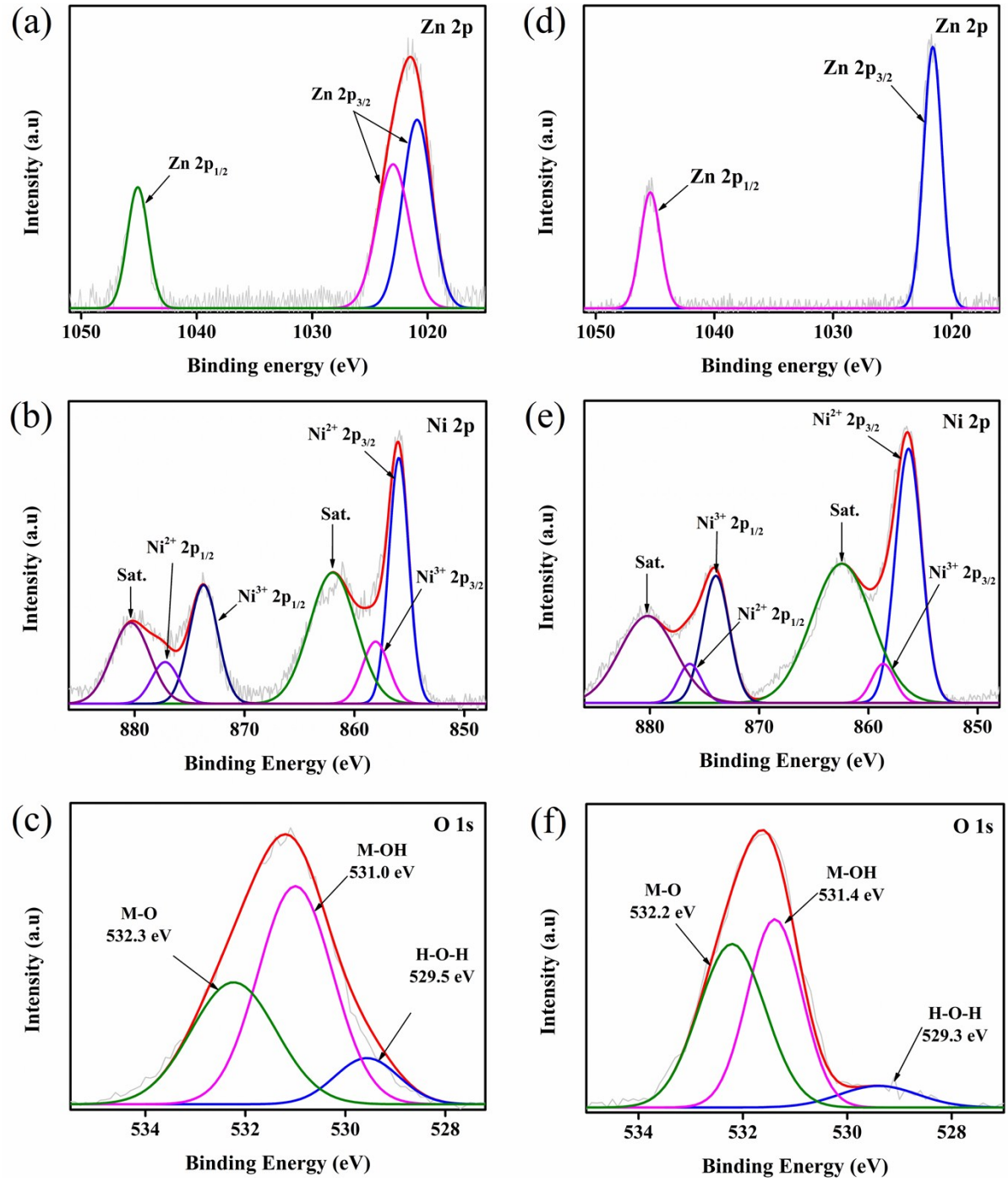

Fig. S5 XPS high-resolution spectra of (a) Zn 2p, (b) Ni 2p, (c) O 1s for Zn-Ni LDH, (d) Zn 2p, (e) Ni 2p, and (f) O 1s for Zn-Ni-O NS arrays.

In case of the Zn-Ni LDH, the high-resolution XPS spectrum of Zn 2p exhibits the main peaks at the binding energies of ~1020.9, 1023.1, and 1045.2 eV, corresponding to Zn $2p_{3/2}$ and Zn $2p_{1/2}$, respectively. The high-resolution XPS spectrum of Ni 2p shows that the binding energies of ~855.9, 858.2 and 861.9 eV, which corresponds to the Ni $2p_{3/2}$ and its satellite

peak, respectively. In addition, the binding energies of ~873.7, 877.2, and 880.2 eV that correspond to the Ni $2p_{1/2}$ and its satellite peak, respectively. The high-resolution XPS spectrum of O 1s displays two strong peaks at ~531 and 532.3 eV, corresponding to the M-OH and M-O bonding. For Zn-Ni-O NS arrays, the Zn 2p deconvoluted into two main peaks at the binding energies of ~1021.6 and 1044.7 eV, corresponding to Zn $2p_{3/2}$ and Zn $2p_{1/2}$, respectively. The Ni 2p deconvoluted into three main peaks at the binding energies of ~856.3, 858.6 and 862.4 eV, corresponding to Ni $2p_{3/2}$ and its satellite peaks, respectively. Besides, the binding energies of ~873.9, 876.3, and 880.1 eV which correspond to the Ni $2p_{1/2}$ and its satellite peak, respectively. The O 1s deconvoluted into two main peaks at the binding energies of ~531.4 and 532.2 eV, corresponding to M-OH and M-O bonding. The binding energies of the Zn 2p, Ni 2p, and O 1s is relatively higher than that of the bulk materials, which further confirms that the high synergistic interaction between Zn-Ni and OH/O in the as-prepared materials (Zn-Ni LDH and Zn-Ni-O NS arrays).

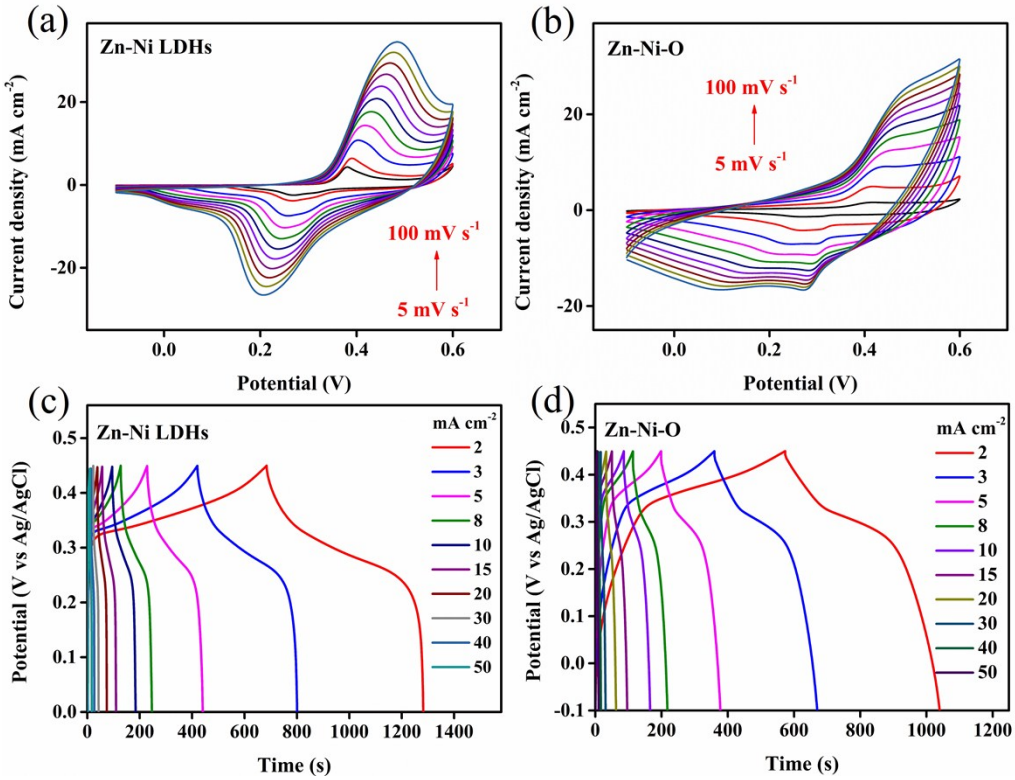

Fig. S6 (a, b) CV curves with different sweep rates, (c, d) GCD curves with different current densities of Zn-Ni LDH and Zn-Ni-O electrodes, respectively.

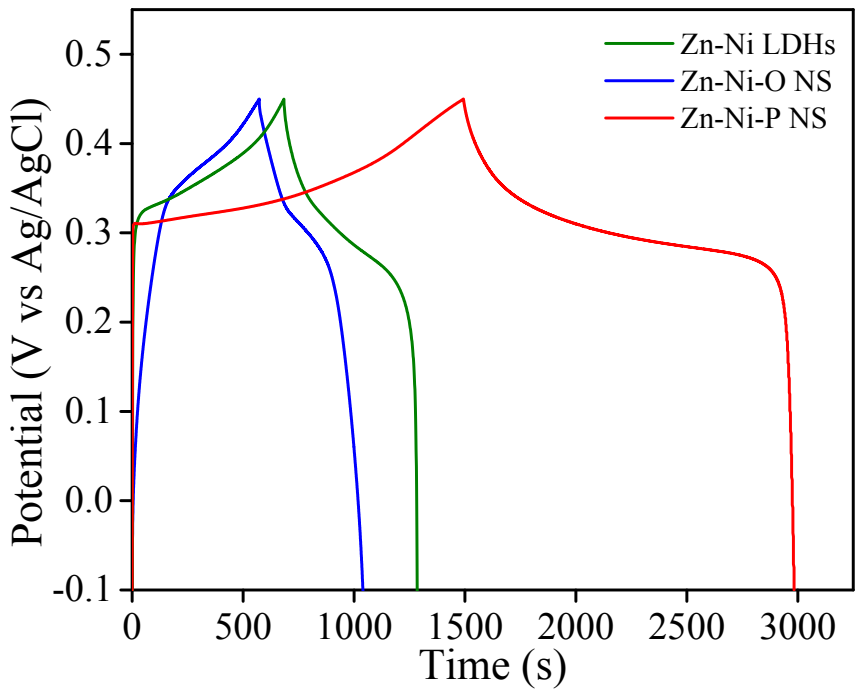

Fig. S7 GCD curves of Zn-Ni LDH, Zn-Ni-O, and Zn-Ni-P electrodes at a constant current density of 2 mA cm^{-2}.

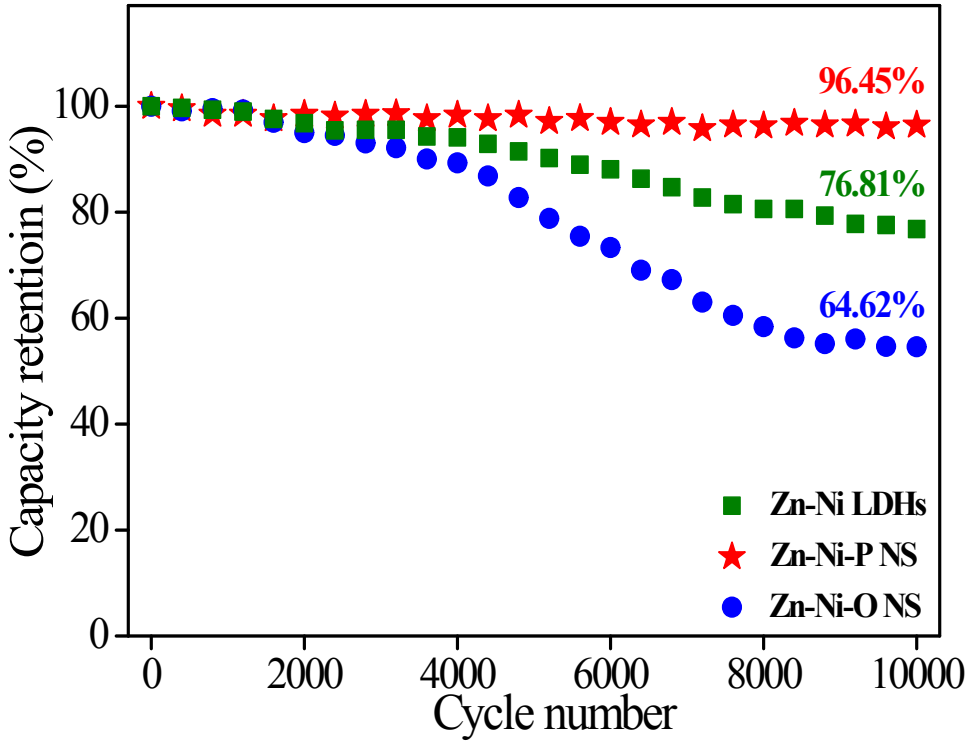

Fig. S8 Cycling performance of Zn-Ni-P, Zn-Ni LDHs, and Zn-Ni-O electrodes at current density of 12 mA cm^{-2}.

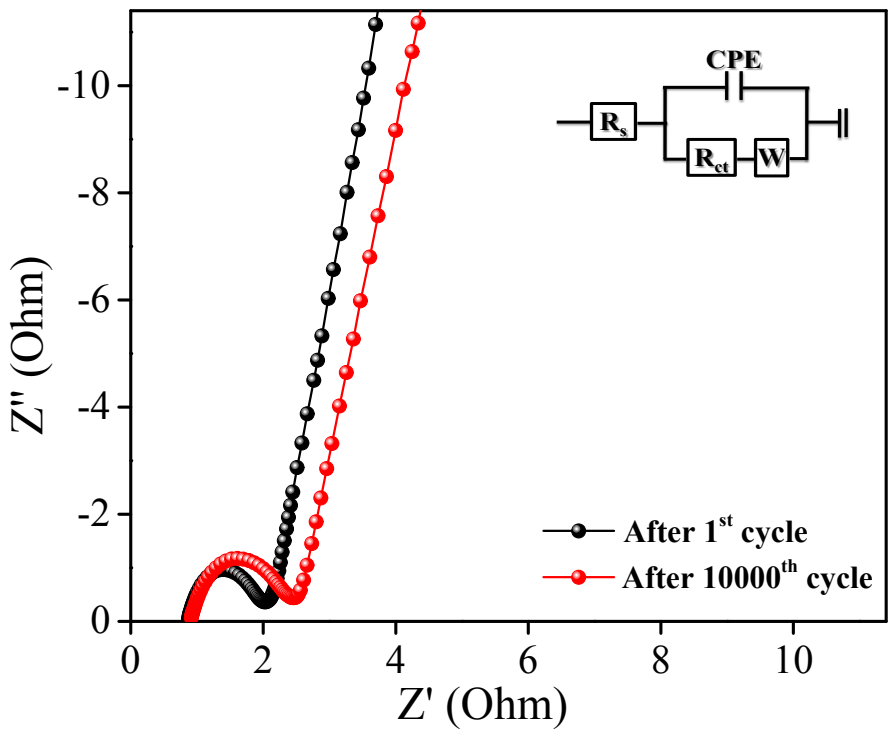

Fig. S9 EIS of Zn-Ni-P electrode during the cycling stability test (Inset shows the equivalent circuit).

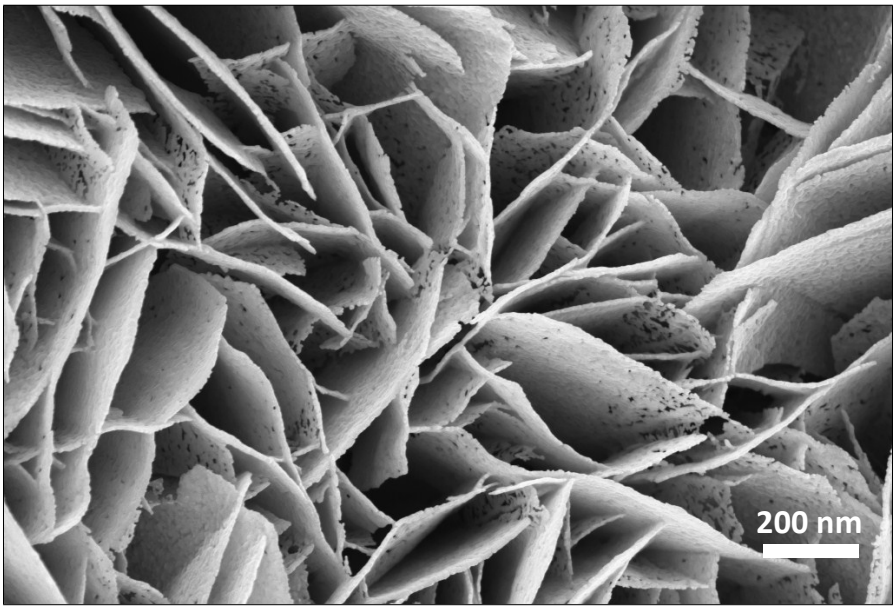

Fig. S10 SEM picture of Zn-Ni-P electrode (after cycling stability tests).

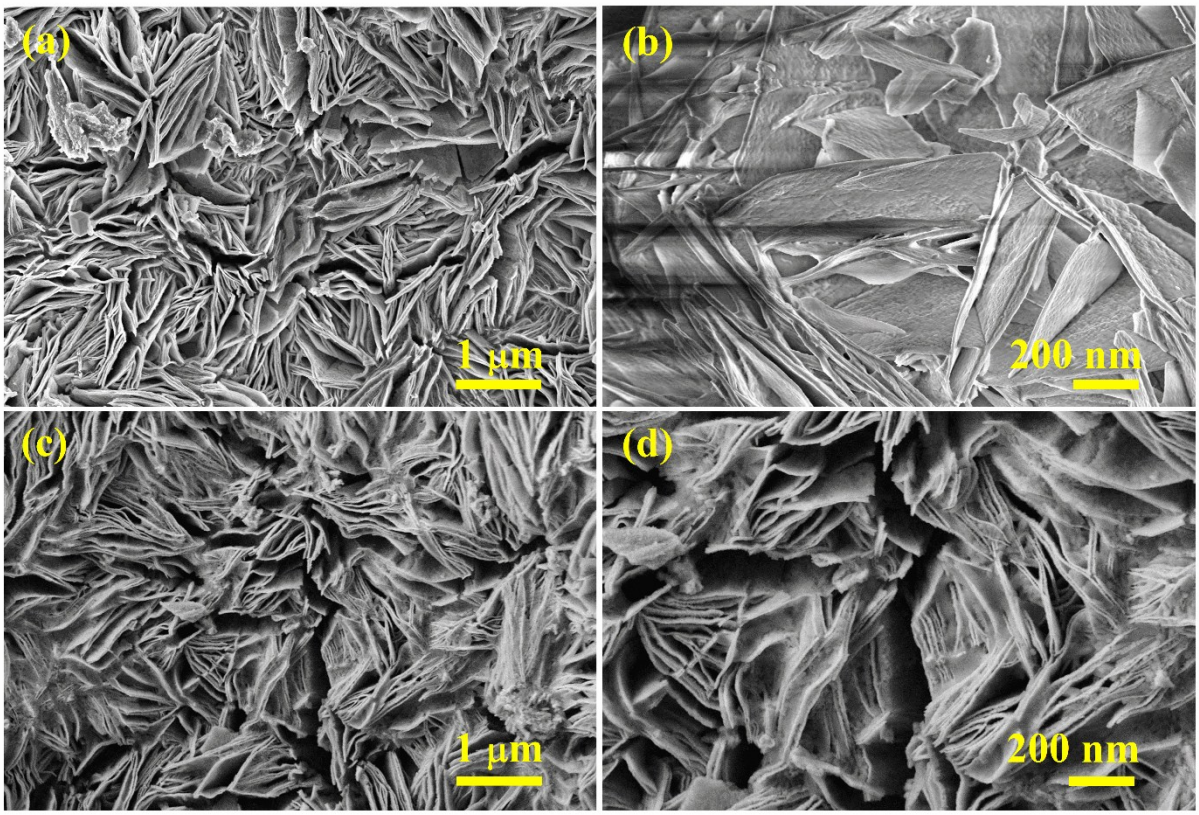

Fig. S11 SEM images with different magnification of (a, b) Zn-Ni LDH, and (c, d) Zn-Ni-O NS arrays (after cycling stability test).

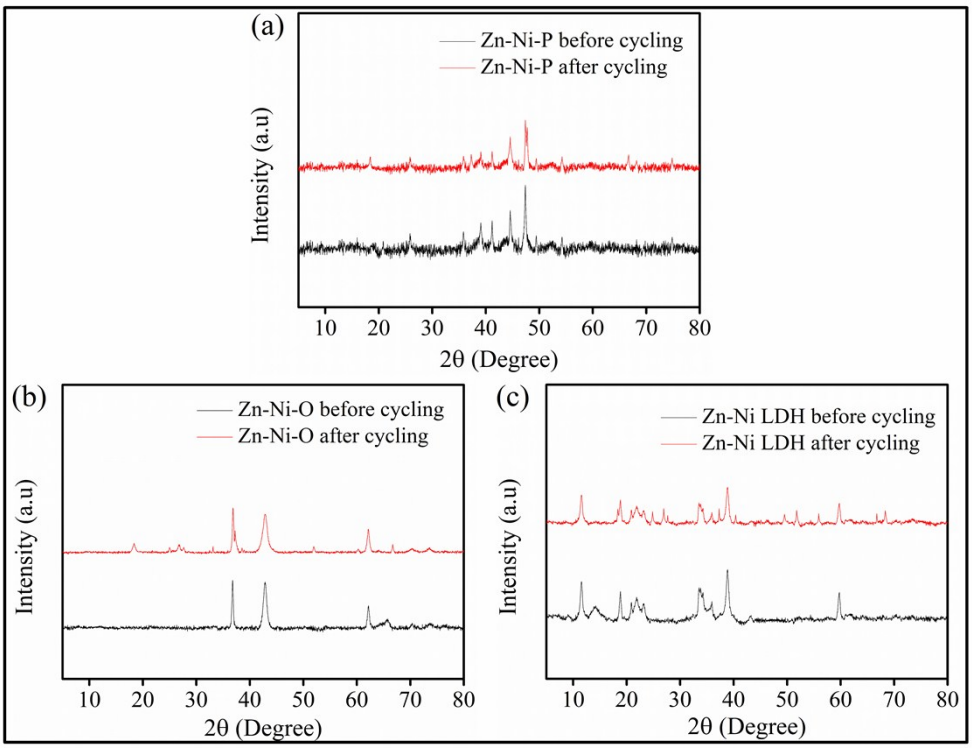

Fig. S12 X-ray diffraction pattern of (a) Zn-Ni-P, (b) Zn-Ni-O, and (c) Zn-Ni LDH electrodes (after cycling stability test).

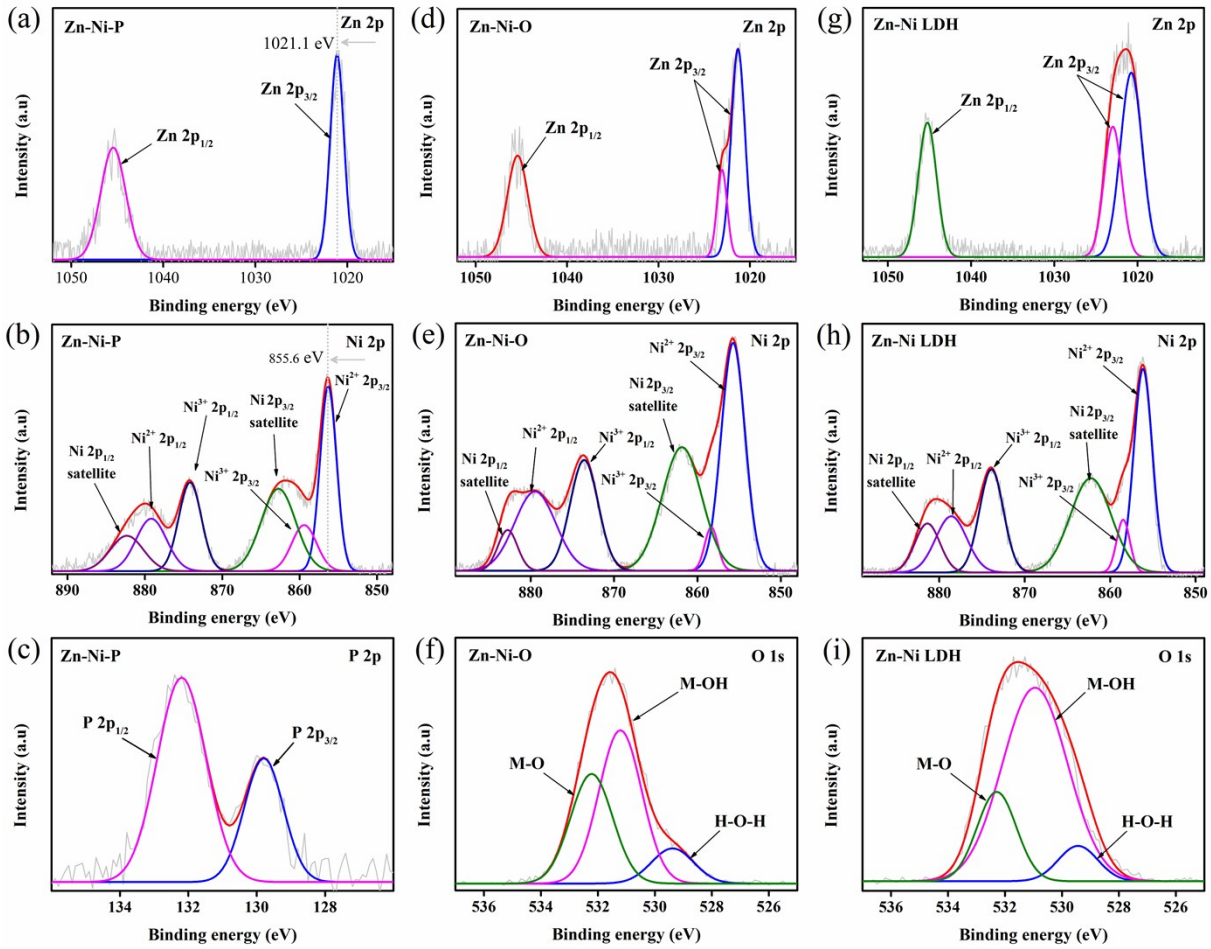

Figure S13. XPS high-resolution spectra of (a) Zn 2p, (b) Ni 2p, (c) P 2p for Zn-Ni-P NS arrays, (d) Zn 2p, (e) Ni 2p, (f) O 1s for Zn-Ni-O NS arrays, (g) Zn 2p, (h) Ni 2p, (i) O 1s for Zn-Ni LDH precursor (after cycling stability test).

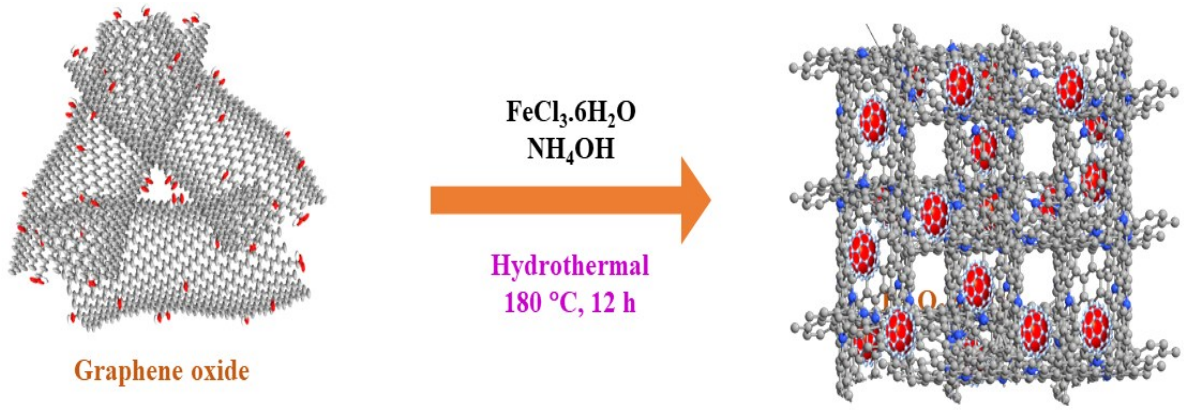

Fig. S14 Schematic illustration for the synthesis of Fe_2O_3@NG hydrogel.

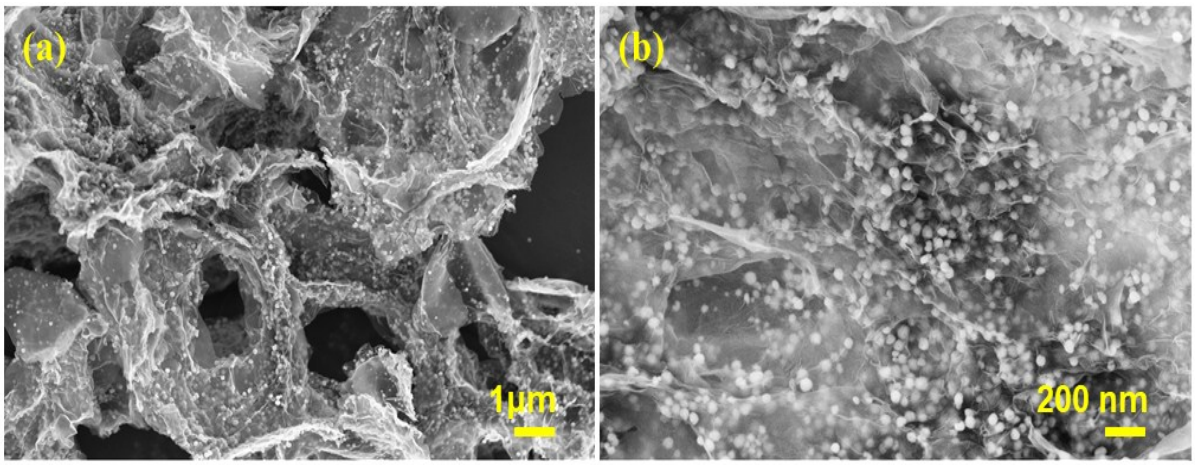

Fig. S15 SEM images with different magnification of the as-synthesized Fe_2O_3@NG hydrogel.

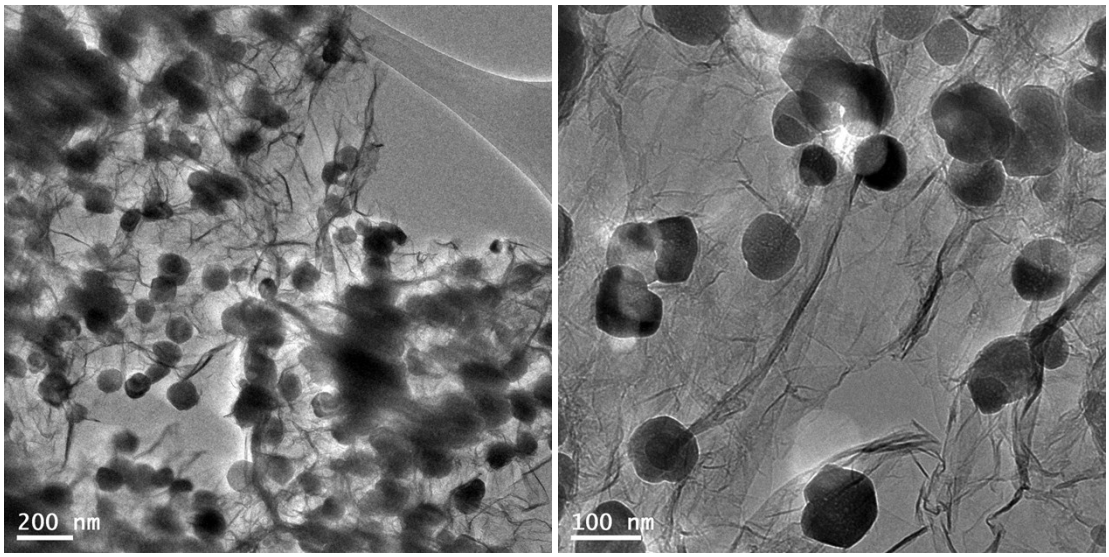

Fig. S16 TEM images with different magnification of as-synthesized Fe_2O_3@NG hydrogel.

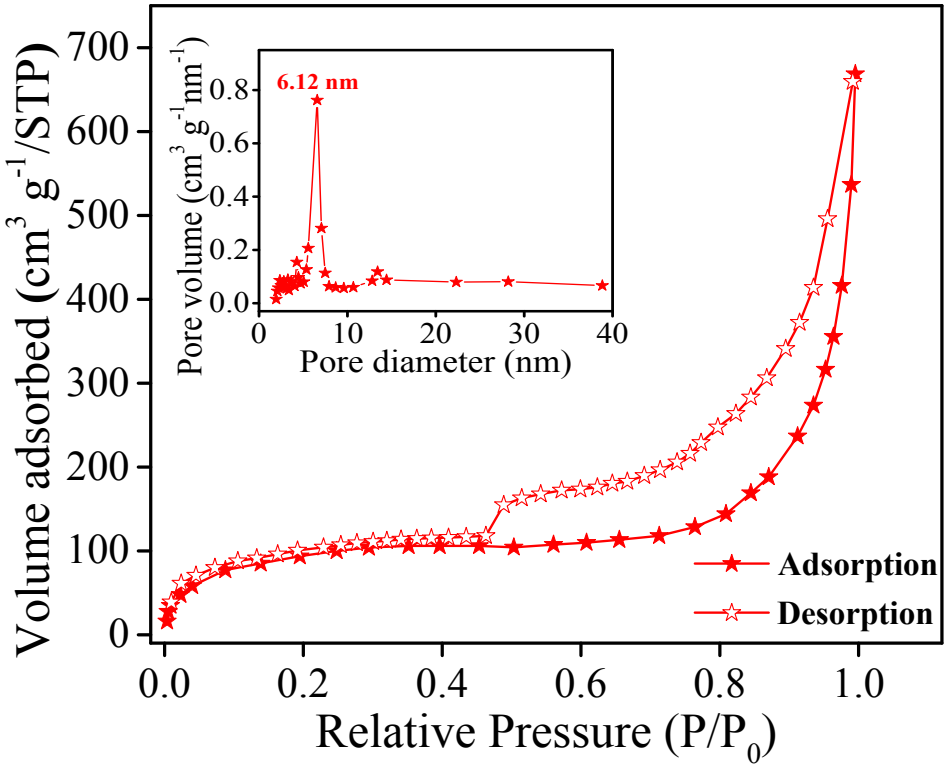

Fig. S17 N_2 sorption isotherm of the as-synthesized Fe_2O_3@NG hydrogel (Inset shows the pore size distribution).

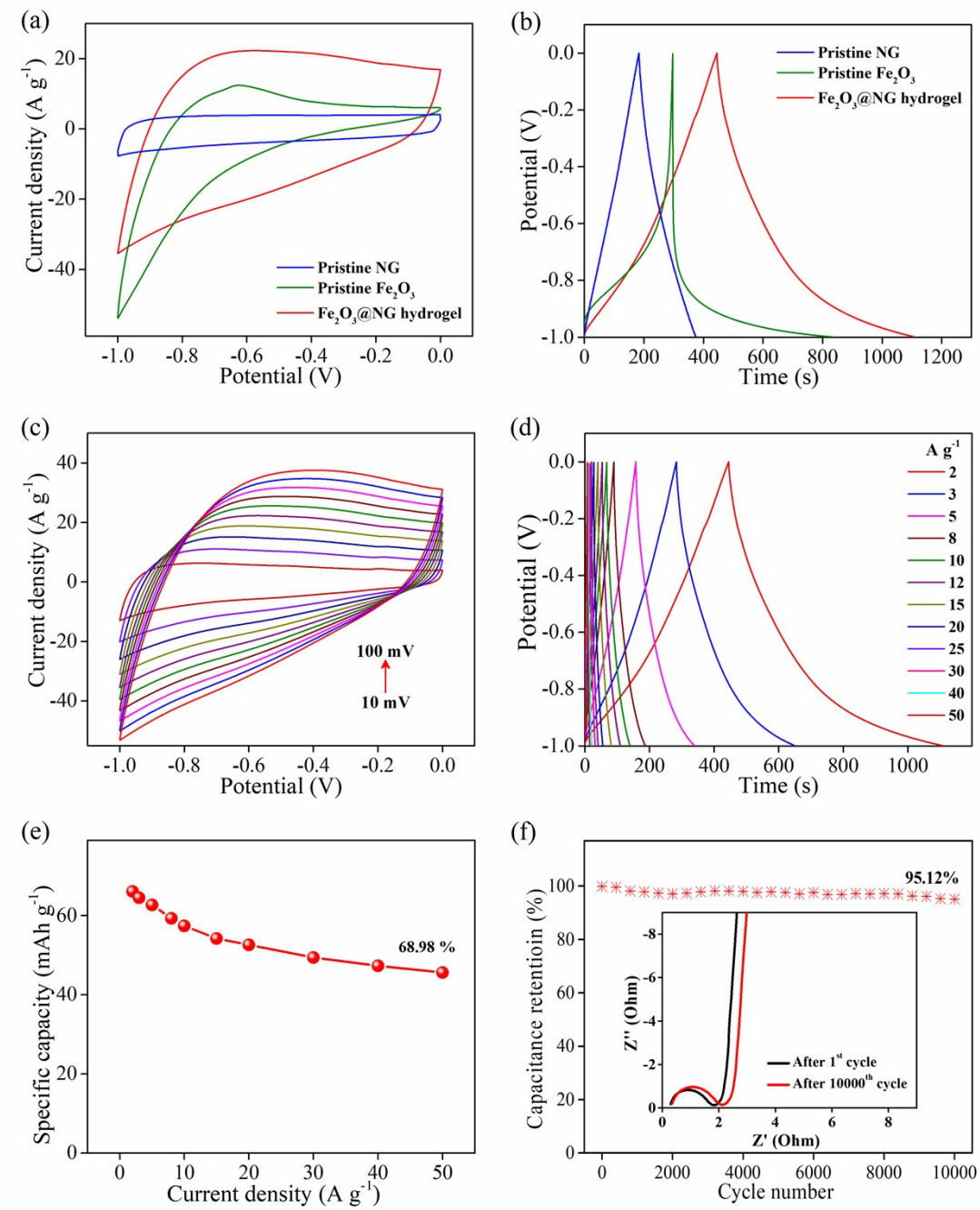

Fig. S18 (a) CV curves of the as-synthesized NG, Fe_2O_3, and Fe_2O_3@NG hydrogel at a scan rate of 50 mV s^{-1}, (b) GCD curves as-synthesized NG, Fe_2O_3, and Fe_2O_3@NG hydrogel at a current density of 2 A g^{-1}, (c) CVs of Fe_2O_3@NG hydrogel at different sweep rate from 10 to 100 mV s^{-1}, (d) GCDs of Fe_2O_3@NG hydrogel at different current density from 2 to 50 A g^{-1}, (e) specific capacity of Fe_2O_3@NG hydrogel at different current densities, and (f) Cycling stability of Fe_2O_3@NG hydrogel (Inset shows EIS of Fe_2O_3@NG electrode during the cycling stability test).

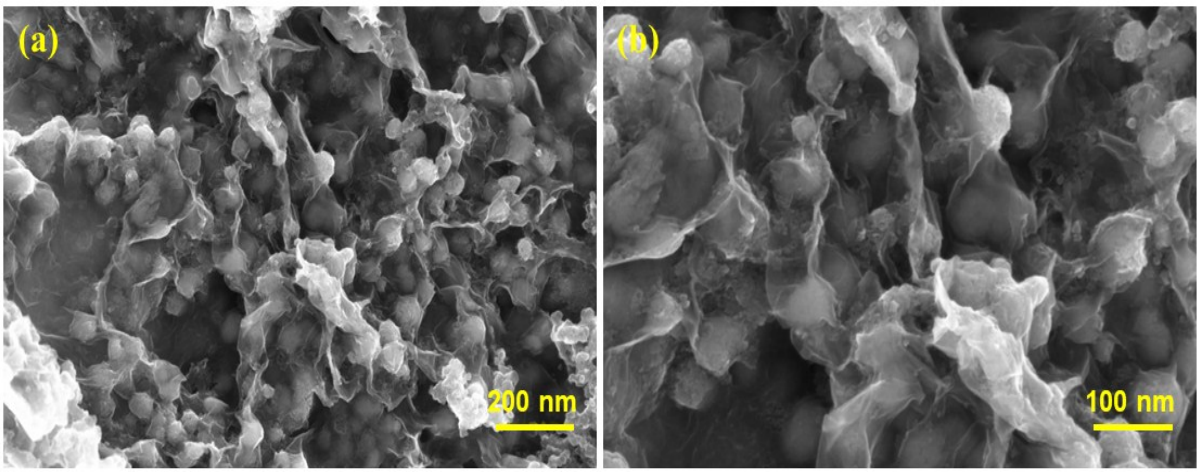

Fig. S19 SEM image of the as-synthesized Fe_2O_3@NG hydrogel (after cycling stability test).

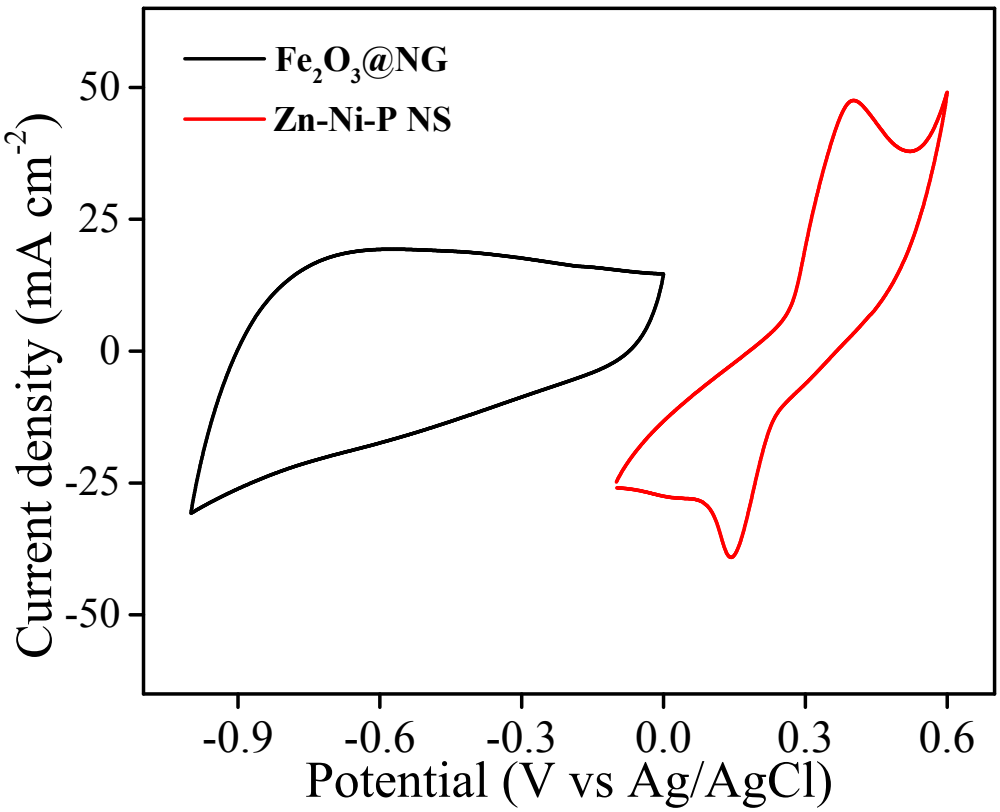

Fig. S20 Fe_2O_3@NG (negative) and Zn-Ni-P (positive) electrodes measured at a constant scan rate of 50 mV s^{-1} in a three-electrode configuration.

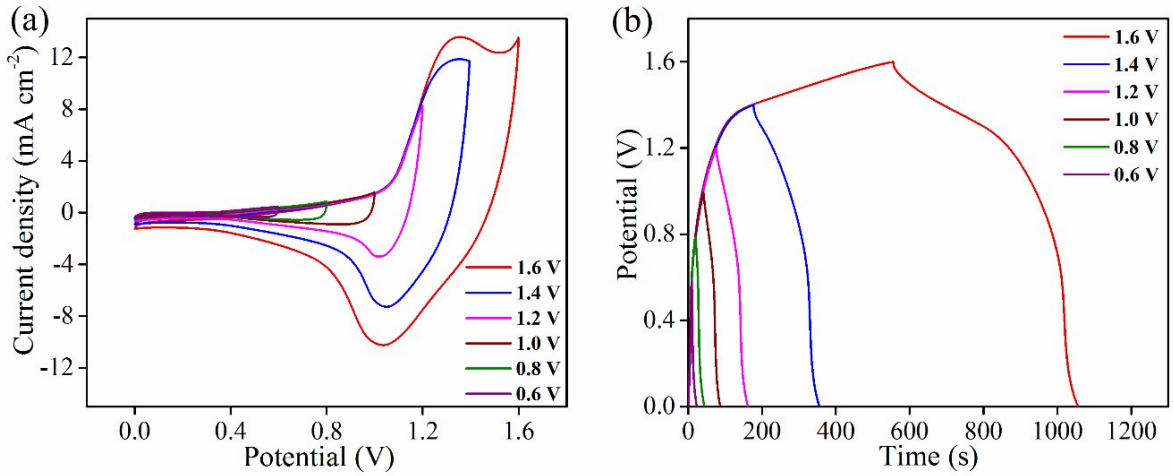

Fig. S21 CV curves (scan rate 50 mV s^{-1}) of the optimized Zn-Ni-P//Fe_2O_3@NG ASC device measured at different potential windows from 0.6 to 1.6 V, (b) GCD curves (at a current density of 3 A g^{-1}) of the Zn-Ni-P//Fe_2O_3@NG ASC device collected at different potential windows from 0.6 to 1.6 V.

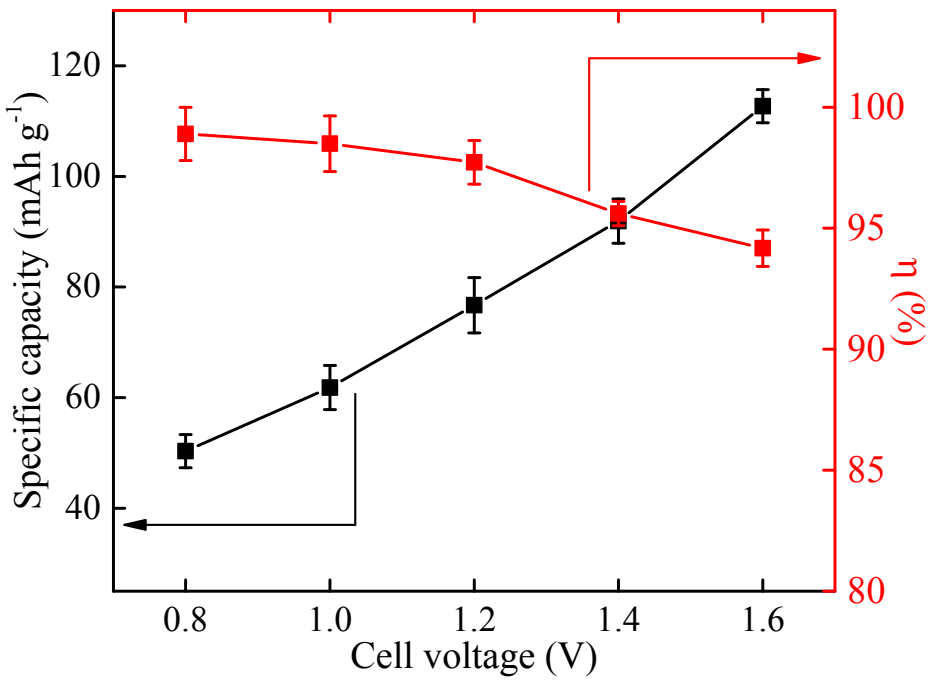

Fig. S22 Coulombic efficiency and specific capacity of the Zn-Ni-P NS//Fe_2O_3@NG ASC device in KOH-PVA electrolyte *vs.* different operating cell voltage.

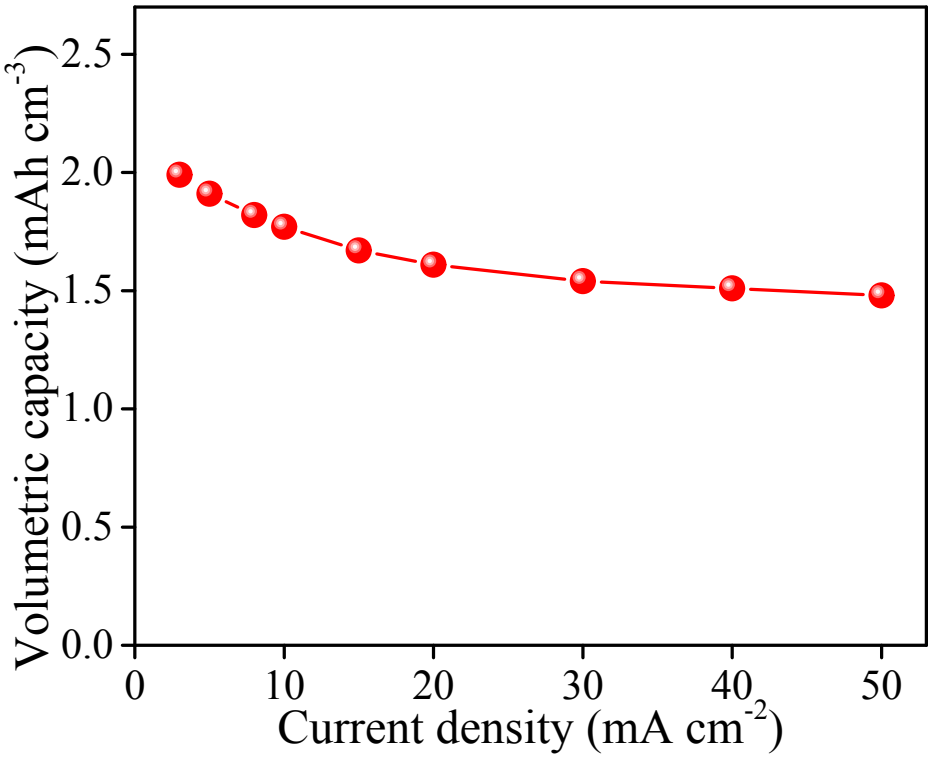

Fig. 23 Volumetric capacity vs. current density of the Zn-Ni-P//Fe_2O_3@NG ASC device.

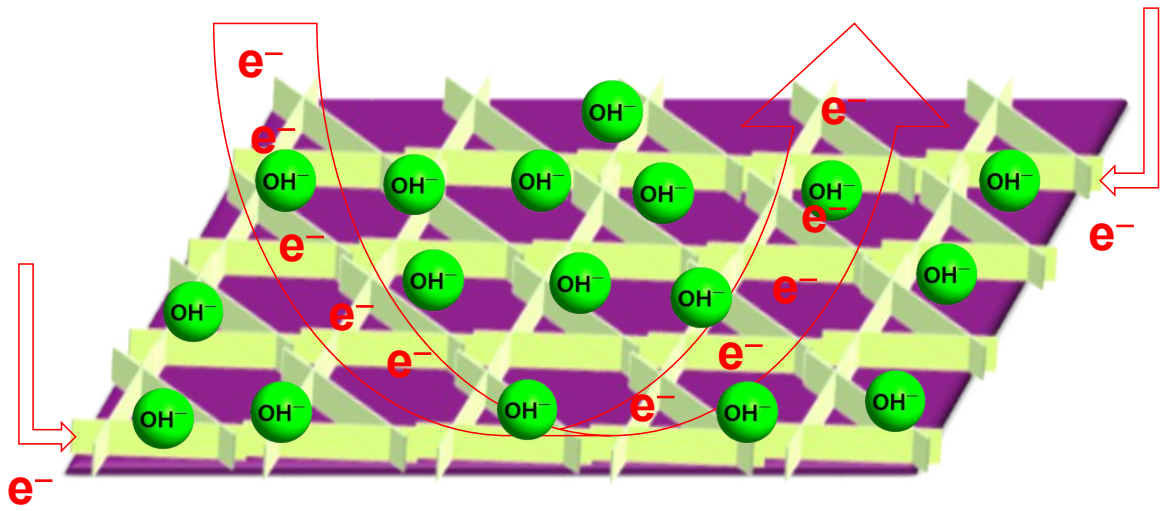

Fig. S24 Schematic of the redox reaction mechanism involved in the high electrochemical properties of the exclusive ion diffusion process.

Table S1. Elemental composition of Zn-Ni LDHs, Zn-Ni-O, and Zn-Ni-P NS arrays estimated by ICP-OES.

Samples	Zn (at. %)	Ni (at. %)	P (at. %)	O (at. %)
Zn-Ni LDHs	19.03	38.72		42.25
Zn-Ni-O NS	17.94	38.31		43.75
Zn-Ni-P NS	18.71	37.06	38.09	6.14

Zn, Ni, P and O contents were detected by ICP-OES.

Table S2. Electrode properties comparison with reported literatures.

Electrode materials	Specific capacitance/ capacity	Current load/ Scan rate	Electrolyte	Stability (Cycles)	References
Ni_2P NS/NF	2141 F g^{-1}	50 mV s^{-1}	6 M KOH	-	1
Amorphous Ni-P	1597 F g^{-1}	0.5 A g^{-1}	2 M KOH	71.4% (1000)	2
NiCoP NS	194 mAh g^{-1}	1 A g^{-1}	1 M KOH	81% (5000)	3
Ni_xP_y	1272 C g^{-1}	2 A g^{-1}	3 M KOH	90.9% (5000)	4
Ni_8-Co_1-P	1448 F g^{-1}	1 A g^{-1}	3 M KOH and 0.5 M LiOH	-	5
Co_2P nanoflowers	416 F g^{-1}	1 A g^{-1}	6 M KOH	-	6
Ni-P@$NiCo_2O_4$	1240 F g^{-1}	1 A g^{-1}	6 M KOH and 0.7 M LiOH	-	7
Ni_2P	843.25 F g^{-1}	1 A g^{-1}	2 M KOH	96% (1000)	8
Ni-Co-S	1418 F g^{-1}	5 A g^{-1}	1 M KOH	-	11
$ZnCo_2O_4$@$Ni_xCo_{2x}(OH)_{6x}$ NWAs	419.1 μA h cm^{-2}	5 mA cm^{-2}	2 M KOH	81.4% (2000)	10
Grass-like Ni_3S_2 nanorod/nanowire	4.52 F cm^{-2}	1.25 mA cm^{-2}	3 M KOH	108.3% (2000)	11
$Ni_xCo_{1-x}O/Ni_yCo_{2-y}P$@C	1.32 F cm^{-2}	1 mA cm^{-2}	1 M KOH	No decay (3000)	12
Zn-Ni-P NS	**384 mAh g^{-1}**	**2 mA cm^{-2}**	**2 M KOH**	**96.45 (10000)**	**This work**

Table S3. ASCs device properties comparison with reported literatures.

System	Electrolyte	Device window (V)	Energy Density (W h kg^{-1})	Power density (W kg^{-1})	Stability (Cycles)	Ref
N_2P NS/NF//AC	6 M KOH	0-1.4	26	337	91.3% (5000)	1
Ni-P//AC	2 M KOH	0-1.6	29.2	400	84.5% (1000)	2
NiCoP//Graphene	1 M KOH	0-1.5	32.9	1301	83% (5000)	3
Ni_xP_y//AC	3 M KOH	0-1.5	67.2	750	84.6% (5000)	4
Ni_8Co_1P//AC	3 M KOH and 0.5 M LiOH	0-1.5	22.8	4320	No decay (5000)	5
Co_2P//Graphene	6 M KOH	0-1.5	8.8	6000	97% (6000)	6
Ni-P@$NiCo_2O_4$//AC	6 M KOH and 0.7 M LiOH	0-1.4	13.3	5700	78.3% (10000)	7
Ni_2P//Fe_2O_3	2 M KOH	0-1.6	35.5	400	86% (1000)	8
Ni-Co-S//Graphene	1 M KOH	0-1.8	60	1800	82.2% (20000)	9
$ZnCo_2O_4$@$Ni_xCo_{2x}(OH)_{6x}$ NWAs//AC	2 M KOH	0-1.7	26.2	511.8	88.2% (2000)	10
Ni_3S_2//NPGC	3 M KOH	0-1.8	48.5	4800	93.1% (5000)	11
Zn-Ni-P//Fe_2O_3@NG	2 M KOH	0-1.6	90.12	611	93.05% (20000)	This work

Notes and References

1. K. Zhou, W. J. Zhou, L. J. Yang, J. Lu, S. Cheng, W. J. Mai, Z. H. Tang, L. G. Li and S. W. Chen, *Adv. Funct. Mater*, 2015, **25**, 7530-7538.
2. D. Wang, L. B. Kong, M. C. Liu, W. B. Zhang, Y. C. Luo and L. Kang, *J. Power Sources*, 2015, **274**, 1107-1113.
3. H. F. Liang, C. Xia, Q. Jiang, A. N. Gandi, U. Schwingenschlogl and H. N. Alshareef, *Nano Energy*, 2017, **35**, 331-340.
4. S. Liu, K. V. Sankar, A. Kundu, M. Ma, J. Y. Kwon and S. C. Jun, *ACS Appl. Mater. Interfaces*, 2017, **9**, 21829-21838.
5. R. Ding, X. D. Li, W. Shi, Q. L. Xu and E. H. Liu, *Chem. Eng. J.*, 2017, **320**, 376-388.
6. X. J. Chen, M. Cheng, D. Chen and R. M. Wang, *ACS Appl. Mater. Interfaces*, 2016, **8**, 3892-3900.
7. X. D. Li, R. Ding, L. H. Yi, W. Shi, Q. L. Xu and E. H. Liu, *Electrochim. Acta.*, 2016, **222**, 1169-1175.
8. D. Wang, L. B. Kong, M. C. Liu, Y. C. Luo and L. Kang, *Chem. Eur. J.*, 2015, **21**, 17897-17903.
9. W. Chen, C. Xia and H. N. Alshareef, *ACS Nano*, 2014, **8**, 9531-9541.
10. W. B. Fu, Y. L. Wang, W. H. Han, Z. M. Zhang, H. M. Zha and E. Q. Xie, *J. Mater. Chem. A*, 2016, **4**, 173-182.
11. T. T. Li, Y. P. Zuo, X. M. Lei, N. Li, J. W. Liu and H. Y. Han, *J. Mater. Chem. A*, 2016, **4**, 8029-8040.
12. L. Wan, J. W. Xiao, F. Xiao and S. Wang, *ACS Appl. Mater. Interfaces*, 2014, **6**, 7735-7742.